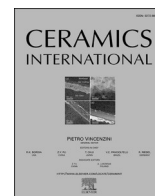




Contents lists available at ScienceDirect

Ceramics International

journal homepage: www.elsevier.com/locate/ceramint

Pure and Ni₂O₃-decorated CeO₂ nanoparticles applied as CO gas sensor: Experimental and theoretical insights

Rafael Aparecido Ciola Amoresi^{a,b,*}, Regiane Cristina de Oliveira^c, Leonélio Cichetto Jr.^d, Paula Mariela Desimone^e, Celso Manuel Aldao^f, Miguel Adolfo Ponce^e, Lourdes Gracia^b, Julio R. Sambrano^c, Elson Longo^d, Juan Andres^b, Alexandre Zirpoli Simões^a

^a School of Engineering, São Paulo State University – UNESP, Guaratinguetá, 12516-410, São Paulo, Brazil

^b Department of Analytical and Physical Chemistry, University Jaume I (UJI), Castelló, 12071, Spain

^c Modeling and Molecular Simulations Group, Sao Paulo State University – UNESP, 17033-360, Bauru, SP, Brazil

^d Functional Materials Development Center, Federal University of São Carlos – UFSCar, São Carlos, São Paulo, Brazil

^e Institute of Materials Science and Technology (INTEMA), University of Mar Del Plata and National Research Council (CONICET), Mar Del Plata, 7600, Argentina

^f Institute of Scientific and Technological Research in Electronics (ICYTE), University of Mar del Plata and National Research Council (CONICET) Juan B. Justo 4302, B7608FDQ, Mar del Plata, Argentina

ARTICLE INFO

Keywords:

CeO₂
Surfaces
Interfaces
Electrical properties

ABSTRACT

In the present work, the structural, morphological and electrical properties of CeO₂ nanoparticles with spherical and rod-like morphologies and rods decorated with Ni₂O₃ were investigated. Morphological, structural and electronic analyses showed a relationship between the shape/size of particles and the respective surface types, number of carriers, density of vacancies and local structural atomic order, in addition to an influence on the electrical properties of the materials. Electrical analyses revealed that the rod-like morphology has a better CO sensor response than the spherical one. In order to complement and rationalize the experimental findings, simulations at the density functional theory (DFT) were carried out to investigate the two possible mechanisms (Langmuir–Hinshelwood and Mars–Van Krevelen) acting on the CO adsorption process and elucidate the behavior of the sensor in heterojunction-type samples.

1. Introduction

Cerium oxide (ceria, CeO₂) is a well-known oxide due to its interesting characteristics, such as electronic mobility and intrinsic non-stoichiometry [1,2]. With a band gap of ~3.2 eV (O_{2p} – Ce_{4f} transitions), CeO₂ is an n-type semiconductor with a face-centered cubic fluorite structure characterized by three low index surfaces (i.e., (100), (110) and (111)), which can be applied, for example, as solid oxide fuel cells [3], photocatalysts [4,5], optical materials [6], UV light blockers [7], and gas sensors [8,9]. However, it is important to recognize that the ideal CeO₂ is not found; in reality, the material has a high oxygen storage capacity since it can easily shift between Ce(IV) and Ce(III), forming bulk and surface oxygen vacancies with consequent high reducibility [10], resulting in the formula CeO_{2-x} [11].

The gas sensor properties of CeO₂ towards CO have been widely explored [9,12–15]. Izu et al. [13] demonstrated that CeO₂ has a faster sensor response to CO gas than SnO₂. Recently, our research group has

been engaged in efforts to obtain and characterize CeO₂ materials applied as CO gas sensor [8,14,16,17]. Such studies resulted in the development of faster synthesis routes to obtain adequate structural crystallinity for CeO₂ [14], in the analysis of the electrical conduction mechanism with dual response – optical and electrical – of the oxide exposed to CO gas [16], and in the improvement of the sensor response when CeO₂ is doped with rare earths [8,17].

Theoretical studies [18–20] have shown that CeO₂ surfaces have different adsorption capacities of the CO gas, from physisorption to surfaces capable to oxidize CO (chemisorption). In addition, the adsorption process can occur in two ways: via Langmuir–Hinshelwood (LH) or Mars–Van Krevelen (MvK) mechanism. In the first model, two molecules participate in the surface adsorption step before reacting, while the product obtained is composed of both molecules previously adsorbed [21]. In contrast, in the MvK mechanism at least one constituent element of the solid lattice participates in the process to form the final product. In other words, some products of the reaction leave the

* Corresponding author. School of Engineering, São Paulo State University – UNESP, Guaratinguetá, 12516-410, São Paulo, Brazil.;
E-mail addresses: rciola@uji.es, rafael.ciola@unesp.br (R.A. Ciola Amoresi).

<https://doi.org/10.1016/j.ceramint.2022.01.286>

Received 26 October 2021; Received in revised form 23 December 2021; Accepted 26 January 2022

Available online 29 January 2022

0272-8842/© 2022 Elsevier Ltd and Techna Group S.r.l. All rights reserved.

solid surface on which they adsorb with one or more constituents from the adsorbate crystalline lattice [22]. It must be mentioned that the most common adsorption processes found for CeO₂ take place through the MvK model [19,23]. Nolan et al. [19] reported that the interaction between CO and CeO₂ (111) surfaces is weak, while on the (110) and (100) surfaces the CO molecule adsorbs strongly. However, according to Oliveira et al. [24] for gas sensor materials the surface with the best adsorptive capacity does not necessarily represent the best sensor response. They showed that surfaces with intermediate adsorptive capacity of the gas of interest allow the reversibility of the sensor response and prevent the poisoning of active sites. Likewise, Lanna et al. [25] demonstrated that the geometry of the CeO₂ surface has a key role in the pathway selectivity for the molecules.

Previous studies on the gas sensor response of CeO₂ nanoparticles towards CO showed correlation among defects, oxygen vacancies and Fermi level alignment [8,17,26]. This behavior can be associated with the easy release of oxygen from the cubic fluorite-type structure, which is well known for its oxygen ion migration properties accompanied by the reversible reduction of Ce(IV) to Ce(III). It was shown that the electrical resistance decreases in response to the presence of CO gas when the material presents an increase in the number of oxygen vacancies, with a subsequent reduction process to yield Ce(III) [26].

Heterojunction engineering allows the creation and control of the presence of defects in the materials. The coupling of two distinct semiconductors to obtain heterojunctions of different types (types I, II and III) and conductivities (p-n, p-p, n-n) leads to changes in the magnetic, electrical, optical and sensor behavior of the materials [27]. Thus, the control of the material surface combined with the formation of heterojunctions permits the Fermi level alignment and the proportion of Ce(III) since CeO₂ has good oxygen mobility and storage capacity, besides the fact that the electrons are transferred between the materials [28]. These electronic transfer processes on the surface of a heterojunction alter the adsorption behavior of gases, increasing its sensor response [29], or changing the selectivity of the gas of interest [30]. Therefore, it is safe to affirm that the sensing properties of heterojunction-type materials is related to the number of defects, surface area and oxygen vacancies; however, little is known about the behavior of the heterojunctions at the atomic level.

The formation of heterojunctions with specific surfaces that interact with CeO₂ is an important strategy to further optimize their adsorption capacity, and consequently their sensor response [31,32]. To this end, studies based on nickel oxide heterojunctions have shown advances in catalytic processes at low temperatures [33]. Nickel can form three different oxides: NiO with a cubic structure, NiO₂ with a monoclinic structure and Ni₂O₃, an unstable and rare oxide-type with a hexagonal structure [34,35] that can be obtained at a specific pressure and temperature [36], by stabilization along the growth process on the surface of oxides [37], or through the use of growth drivers [38]. Ni₂O₃ has a direct band gap in the 2.2–3.4 eV range [34,39], and its structure has space group P63mc and parameters $a = 3.26 \text{ \AA}$ and $c = 5.61 \text{ \AA}$ [36], besides tetrahedrally coordinated Ni (III) cations. For such reasons, this material presents itself as a promising gas sensor [40,41]. Additionally, this type of nickel oxide coupled with CeO₂ [42] has shown catalytic performance towards carbon-based compounds.

This work reports the electrical properties of pure CeO₂ nanoparticles and those decorated with Ni₂O₃ towards CO gas detection. These nanoparticles were synthesized by the microwave-assisted hydrothermal (MAH) method. Here, the term "decorated" was used to refer to the type of microstructure in the heterojunction since different structure junctions are designated according to the way they are built, that is, core/shell, obtained in the form of a core from a structure and a cover from another structure; layer-by-layer, when layers of different structures are grown on top of each other; and decorated-type, in which there is a main structure, and occasionally at some points a second structure is grown. The structural, electronic, optical and electrical properties were correlated with the heterojunction obtained. High-

resolution transmission electron microscopy (TEM), X-ray diffraction (XRD), micro-Raman scattering spectroscopy, ultraviolet–visible (UV–vis) spectroscopy, and X-ray photoelectron spectroscopy (XPS) were employed to characterize the samples in detail. Computational simulations were performed with periodic density functional theory (DFT) to study the structural characteristics, density of states (DOS) and adsorption properties to reach a deep understanding on the relationship between the structural and electronic parameters of pure and Ni₂O₃-decorated CeO₂ nanoparticles.

2. Materials and methods

2.1. Synthesis

Pure CeO₂ samples: The nanoparticles were obtained by the MAH method. The procedure for the preparation of pure CeO₂ samples consisted of dissolving cerium precursor (Ammonium cerium (IV) nitrate [Ce(NH₄)₂(NO₃)₆, 99.9%, Aldrich] for the spherical sample, and nitrate hexahydrate [Ce(NO₃)₃·6H₂O, 99%, Aldrich] for the rod-like sample), 0.06 mol L⁻¹, in 90 mL of NaOH, 6.0 mol L⁻¹, under vigorous stirring at 25 °C for 1 h. The suspension was then placed in a microwave oven at 180 °C/1 min. The powders were washed with deionized water several times and dried at 70 °C/12 h.

Decorated rod-like sample: To obtain the decorated rod-like CeO₂ sample, nickel nitrate (Ni(NO₃)₂·6H₂O, 99.9%, Aldrich) and NaOH (0.1 mol L⁻¹) were used as precursors. A ratio of 5.0 (w/w)% Ni to rod-like CeO₂ was used. The preparation procedure was similar to that for the obtention of pure CeO₂ samples: nickel nitrate was dissolved in 90 mL of NaOH, 0.1 mol L⁻¹, and then added to the CeO₂ particles under vigorous stirring at 25 °C for 1 h. The suspension was subsequently placed in a microwave oven at 140 °C/4 min. The powders were washed with deionized water several times and dried at 70 °C/12 h. As it was not our intention to change the initial morphology of the CeO₂ precursor particles, we opted for the lowest temperature in the microwave and the lowest concentration of NaOH for the synthesis of decorated CeO₂ particles.

2.2. Characterization

The nanoparticles were structurally characterized via XRD patterns using a D/Max-2000PC diffractometer (Rigaku, Japan) with Cu K α radiation ($\lambda = 1.5406 \text{ \AA}$) in the 2θ range from 20° to 60°. The Raman spectroscopy characterization was performed by a LabRAMiHR550 Horiba JobinYvon spectrometer with a 514-nm laser as the excitation source and a spectral resolution of 1 cm⁻¹, with 40 scans in the range of 200–900 cm⁻¹. The particle morphology was investigated via HR-TEM, TEM-FEI/PHILIPS CM120 microscopy and field emission scanning electron microscopy using an Inspect F50 microscope (FEI Company, Hillsboro, OR) operating at 5 kV. Samples for TEM were obtained by drying droplets of the as-prepared samples from an ethanol dispersion, which was sonicated for 5 min onto 300 mesh Cu grids. X-ray photoelectron spectroscopy (XPS) measurements were carried out on a commercial spectrometer (UNI-SPECS UHV System). The spectra were corrected to the charge effects using the C 1s peak of adventitious carbon at 285.0 eV as a reference. All data analyses were made using CASA XPS software (Casa Software Ltd., U.K.). The Mg K α line was used ($h\nu = 1253.6 \text{ eV}$), and the analyzer pass energy was set to 10 eV. The inelastic backgrounds of the Ce 3d, O 1s, and Ni 2p electron core-level spectra were subtracted using Shirley's method. For Ce 3d peak fitting the doublets were separated by 18.5–18.6 eV, FWHM varied between 2.5 and 3.6 eV, and line shapes were adjusted using Gaussian–Lorentzian curves. The photonic characteristics were analyzed by UV–vis diffuse reflectance using a PerkinElmer UV/vis/NIR Lambda 1050 spectrophotometer.

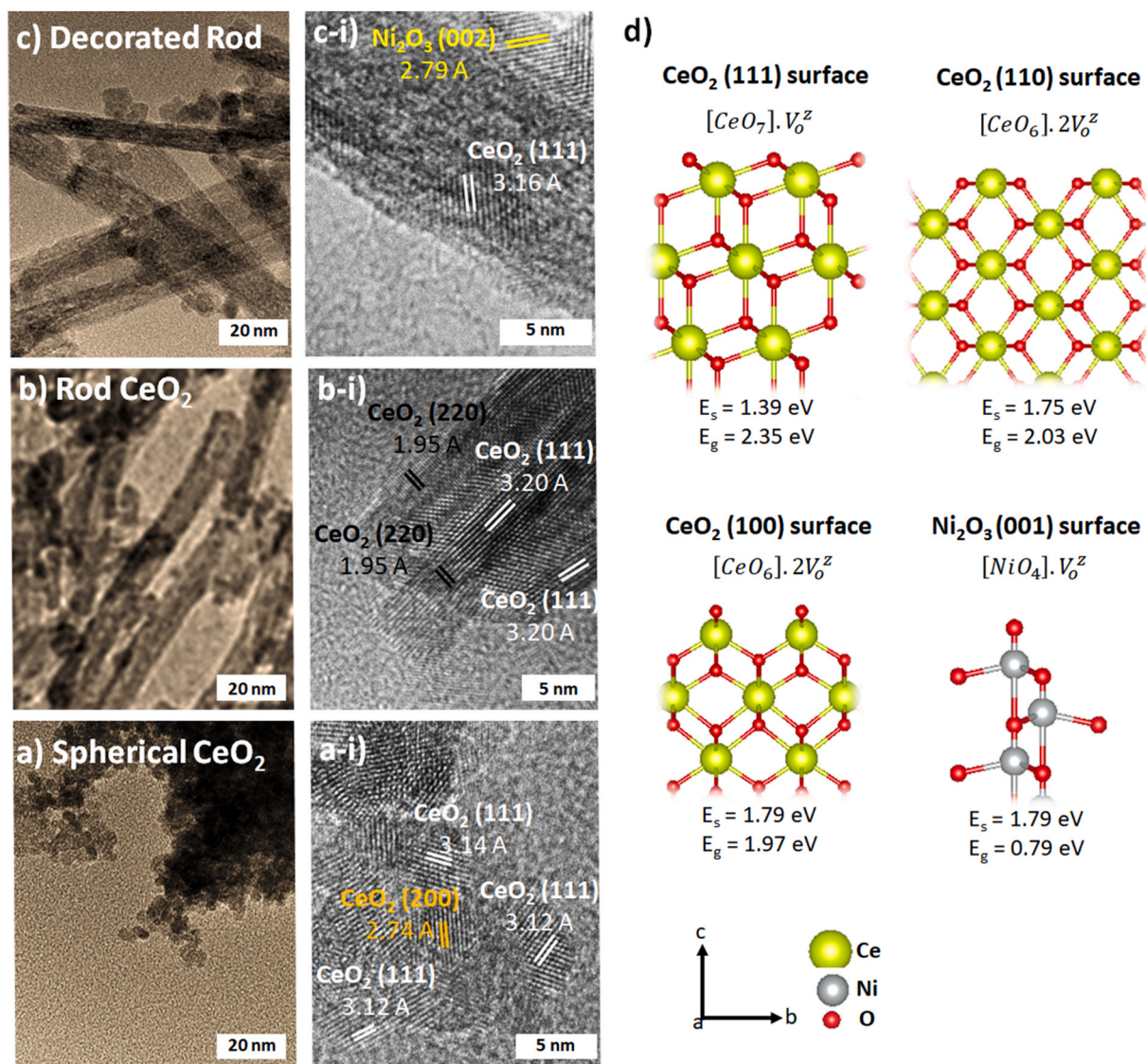


Fig. 1. TEM (a–c) and HR-TEM (i–iii) images of pure (a,b) and decorated (c) CeO₂ samples. Figure d shows the coordination of each surface experimentally obtained from DFT simulations.

2.3. Electrical analyses

For gas-sensing measurements, powder paste was prepared with glycerol as an organic binder. The solid/organic binder ratio used was ½ without dopant addition. A silicon wafer was used as a substrate, and an adhesion layer consisting of 25 nm of titanium was deposited on it. Then, a 200 nm-thick platinum film used as an electrode was deposited onto the Ti layer, and an interdigitated shape was made by sputtering. The interelectrode distance was 50 μm. Thick and porous film samples were painted onto the resulting substrate. After painting, the samples were kept in a conventional oven at 100 °C for 24 h in air for glycerol evaporation and improved adhesion of films to the silicon substrate. Afterwards, the samples were thermally treated at 380 °C for 1 h in air atmosphere at a heating rate of 1 °C/min, and after this treatment the gas-sensing measurements were finally carried out. The measurements were made in a chamber under temperature, pressure and gas composition control. The electrical resistance was measured with an Agilent 3440A multimeter. First, three heating and cooling cycles were carried out in presence of air (1 atm), vacuum (10⁻⁴ atm) and carbon monoxide (0.0066 atm) in order to investigate the performance of the films at certain temperatures in these three different atmospheres. Then, the

electrical resistance was measured in air, vacuum and carbon monoxide (0.0066 and 0.066 atm) for 10 min at each atmosphere at 380 °C and 420 °C.

2.4. Computational methods

Our ab initio simulations were based on DFT calculations using the VASP code [43,44]. The generalized gradient approximation (GGA) formulation with Perdew-Burke-Ernzerhof (PBE) exchange-correlation functional [17] was used. The Ce core is [Xe], whereas C and O cores are [He] and Ni core is [Ar]. All calculations were performed at the DFT + U level with U values of 5.0 eV and 5.3 eV for f-Ce and d-Ni [18,45,46], respectively. CeO₂ surfaces with $p(1 \times 2)$ expansions were then modelled with a finite thickness slab model of (111) surface of 10.92 Å (13 atomic layers). Based on previous works [47,48], the (001) surface of Ni₂O₃ was built with thickness slab of 13 Å (8 atomic layers). To eliminate the slab-slab interaction perpendicular to the surface, a 15 Å vacuum between adjacent slabs was used. $3 \times 3 \times 1$ Monkhorst-Pack grid in *k*-space was used, and all ionic positions were allowed to relax. The surface energy (E_{surf}) was obtained by Eq. (1):

Table 1

Summary of the results obtained by TEM and DFT.

Sample	TEM		DFT		
	Average diameter (nm)	Surfaces	Surface coordinate	E_{surf} (eV)	E_{gap} (eV)
Spherical	4.0 (± 0.1)	(111)	[CeO ₇ , V _o ²⁻]	1.39	2.35
		(100)	[CeO ₆₋₂ , V _o ²⁻]	1.79	1.97
Rod	9.1 (± 0.3)	(111)	[CeO ₇ , V _o ²⁻]	1.39	2.35
		(110)	[CeO ₆₋₂ , V _o ²⁻]	1.75	2.03
Decorated rod	11.4 (± 0.3)	(111)	[CeO ₇ , V _o ²⁻]	1.39	2.35
		(001)	[NiO ₄ , V _o ²⁻]	1.79	0.79
		Ni ₂ O ₃			

$$E_{surf} = \frac{E_{slab} - nE_{bulk}}{2A}, \quad (1)$$

where E_{slab} and E_{bulk} correspond to the optimized total energies of the surface and bulk, respectively, n is the number of CeO₂ units on each surface, and A is the surface area. In order to simulate the experimental sample of the CeO₂ decorated with nickel oxide, a Ni₂O₃ cluster was placed on the (111) surface. For the adsorption process, the adsorbates (CO and O₂ molecules) were placed at an initial distance of 2.0 Å from the substrate surface sites (that is, (111) CeO₂ or heterojunction surfaces) using relaxed coordinates. The adsorption mechanisms of the adsorbates on the substrates were followed by the evaluation of the adsorption energy, E_{ads} , as shown in Eq. (2):

$$E_{ads} = E_{tot} - E_{slab} - E_x, \quad (2)$$

where E_{tot} is the total energy of the surface system with adsorbate, E_{slab} is the energy of the clean substrate, and E_x is the energy of the adsorbate [49]. Using this notation, a negative sign of E_{ads} indicates that the adsorption is a favorable process with a decrease in energy compared to separated adsorbates and substrate surfaces.

3. Results and discussions

3.1. Structural and morphological characteristics

TEM analyses were performed (Fig. 1) in order to elucidate the type of morphology of the pure CeO₂ samples as well as the heterojunction formation. According to the TEM images in Fig. 1a, b and c, it is possible to observe that the pure CeO₂ samples present spherical and rod-like morphologies, while the CeO₂ sample decorated with nickel oxide exhibits a rod-like morphology, respectively. The respective HR-TEM images are shown in the ‘i’ Figures. The high-resolution analysis of the spherical sample (Fig. 1i-a) revealed interplanar distance values of 3.12 Å and 2.74 Å, which are in good agreement with d-spacing (111) and (200) planes of cubic CeO₂, respectively. In this sample there is a predominance of the (111) surface. For the rod-like CeO₂ sample, the HR-TEM image (Fig. 1i-b) showed calculated interplanar distances of 1.95 Å and 3.22 Å, which are consistent with d-spacing (220) and (111) planes of cubic CeO₂, respectively. Finally, for the decorated rod-like CeO₂ sample (Fig. 1c) the same morphology as the pure sample can be observed, but with cubes formed on them. According to Fig. 1i-c, the interplanar distance of these cubes was 2.79 Å, which can be assigned to the (002) plane of the Ni₂O₃ hexagonal phase (JCPDS Card number 14-0481).

A coherent growth is estimated between the CeO₂ and Ni₂O₃ interfaces, provided that the CeO₂ cubic structure has a lattice parameter equal to 5.46 Å, while the hexagonal nickel oxide has a parameter $c = 5.61$ Å, which results in a mismatch of the 2.7%. In order to corroborate the formation of the Ni₂O₃ phase, duplicates of other samples synthesized by the same methodology were analyzed (Fig. S1). The presence of the element nickel in the pure sample was confirmed by EDS (Fig. S2). The growth of nickel oxide in only regions of the CeO₂ surface characterizes the formation of a heterojunction designated as decoration (“decorated rods”). The surfaces found in the TEM analyses were simulated by DFT, as shown in Fig. 1d. It is possible to observe the coordination of each surface, their surface energy, E_{surf} (Eq. (01) – section 2.4), and their band gap, E_{gap} , both obtained from DFT simulations. Table 1 presents a summary of the results obtained by TEM (types of

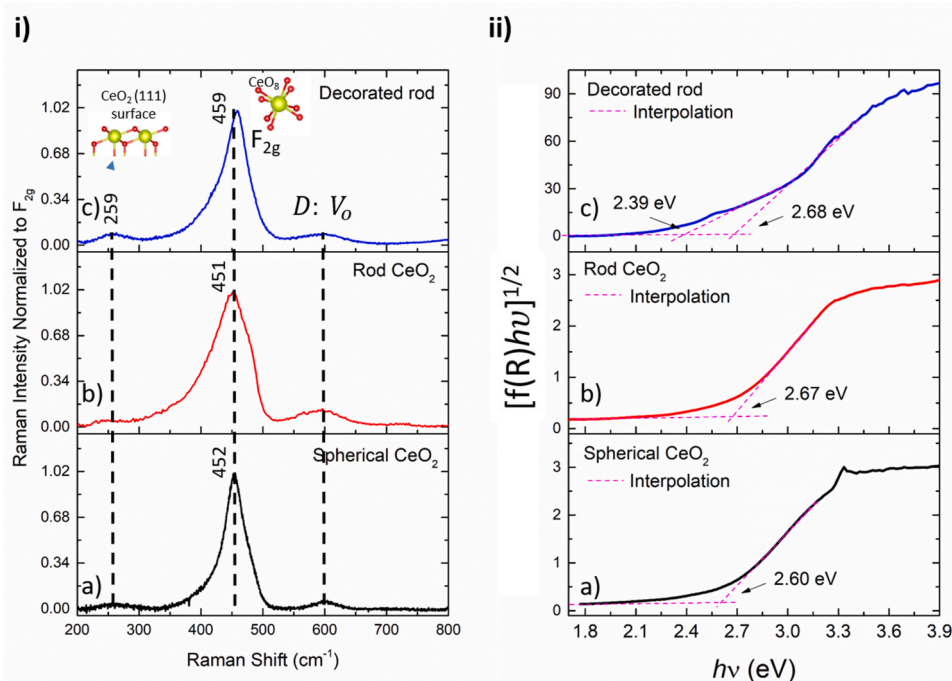


Fig. 2. a) Raman spectra of the structural properties of pure and decorated CeO₂ samples at short-range order and b) optical band gap of the samples.

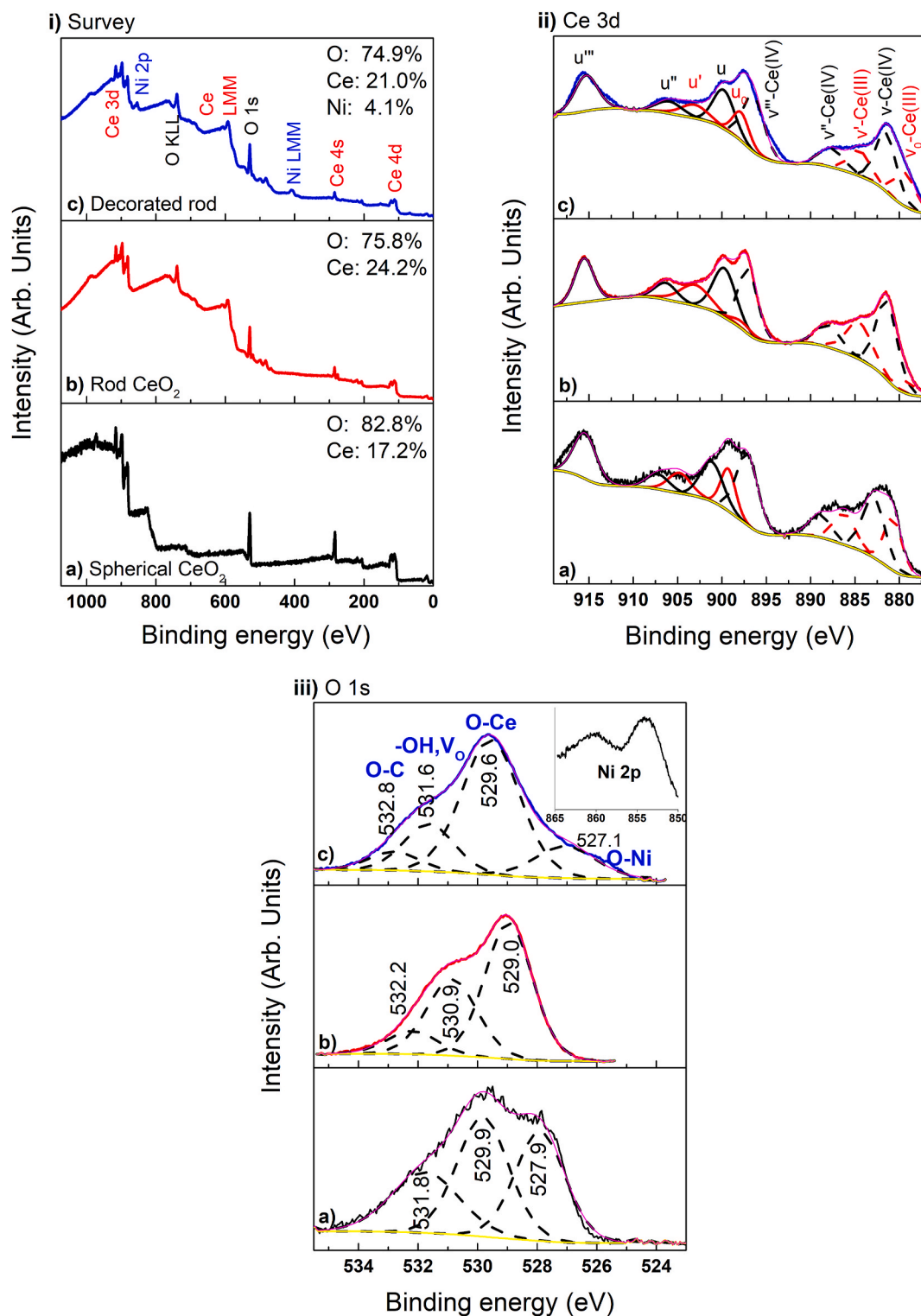


Fig. 3. XPS spectra of spherical (Figures a), rod-like (Figures b) and decorated rod-type (Figures c) CeO₂ samples. The survey spectra, the Ce 3d and the O 1s peaks are shown in i), ii) and iii), respectively. The inset in iii-c displays the high-resolution spectra of Ni 2p.

surfaces found and particle average diameter shown in Fig. S4) and DFT (surface coordinate, surface and band gap energy). The vacancy type V_{O}^{\bullet} means that the surface can take on the V_{O}^{\bullet} , V_{O} , or V_{O}^{\ominus} types.

Fig. S3 displays the XRD analyses of the nanoparticles obtained. It can be observed that both samples present a cubic polycrystalline structure of CeO₂ with space group $Fm\bar{3}m$ corresponding to ICSD no. 239412. For the decorated rod-like sample, no peaks related to the

nickel oxide phase can be noted, which is acceptable due to the synthesis method used – since neither the formation of a conventional solid solution (given that the CeO₂ precursor has a crystalline structure) nor a second phase can be obtained as a result of the low concentration of the junction with nickel oxide [50]. Table S1 shows the Rietveld refinement of the diffractograms. The fitting parameters (wR (%)) obtained using GSAS-II software and ICSD no. 239412 indicate good agreement

between the calculated and observed XRD patterns for the as-prepared CeO₂ nanocrystals. According to this crystallographic data, CeO₂ has a lattice parameter value of 5.46 Å, which is congruent with the values presented by our samples. An analysis of the refinement results renders that the rod-like CeO₂ sample has reduced cell volume in relation to the other two samples. A comparison between the pure and decorated rod-like samples shows an increase in the lattice parameter, probably caused by the high density of vacancy-type defects.

Phase formation and structural defects of the nanoparticles at short-range order were investigated by Raman spectroscopy. The active Raman mode near 465 cm⁻¹ corresponds to the triply degenerate F_{2g} symmetric stretching of Ce–O bonds in the [CeO₈] unit [51]. For the pure CeO₂, the presence of oxygen defects and Ce (III) cations changes the length of the Ce–O bonds, shifting the center of the F_{2g} mode to different wavenumber when compared to the 465 cm⁻¹ value of the single crystal [52]. According to Schilling et al. [53], the band at 240–270 cm⁻¹ is correlated with the second-order acoustic band (2 TA) mode, whereas the one at 600 cm⁻¹ is related to defect (D) modes [53–55]. Some different characteristics are observed for the spectrum of the samples, such as: i) the 260 cm⁻¹ mode is active in spherical (Fig. 2i–a) and decorated (Fig. 2i–c) samples; ii) there are differences in position and shape of the F_{2g} peak between the pure (Fig. 2i–a,b) and decorated (Fig. 2i–c) samples; iii) and the area of the band at 590 cm⁻¹ is different among the samples.

Concerning the band at 260 cm⁻¹, this mode originates from terminations of the (111) surface of the O–Ce longitudinal stretching type of atoms in the outermost layers [53], as verified in the spherical and decorated samples. The band at ~455 cm⁻¹ represents the vibrational mode of the octahedron of Ce–O₈, which is a very sensitive mode to any disordered state in the stoichiometric system. This band is wider for the rod-like sample than for the others. Since the Raman spectra peak

position and bandwidth are influenced by several factors, such as phonon confinement, particle size heterogeneity, defects, non-stoichiometry and lattice stress, as seen by TEM analyses, the different surfaces and nickel oxide decoration result in differences in the band at ~455 cm⁻¹. To better correlate this result, it is necessary to analyze the band at 600 cm⁻¹, which is related to defects. The relative concentration of vacancies can be represented by the ratio of the band area at 600 cm⁻¹, I_D, and at 455 cm⁻¹, I_{F_{2g}}. The resulting sequence is: rods (0.075) > decorated rods (0.056) > spheres (0.046). TEM images showed that the spherical sample is mainly composed of the (111) surface, with seven oxygens coordinated to cerium [CeO₇.V_o], while the rod-like sample is predominantly formed by the (111) and (110) surfaces, with seven and six oxygens coordinated to cerium ([CeO₇.V_o], [CeO₆.2V_o]), respectively. The sequence of concentration of vacancies between samples is logical when two parameters are considered: i) the lower coordination of Ce to O ions in the crystal lattice increases the concentration of vacancies, and ii) the Raman spectroscopy is sensitive to the detection of short-range changes in the chemical bonding. Therefore, the sample composed of surfaces with lower Ce–O coordination will present higher vacancy density. In turn, the decorated rod-like sample presents an intermediate vacancy concentration in relation to the two previous ones. This sample is formed by the (111) CeO₂ surface and the junction with nickel oxide, which leads to this vacancy concentration range according to the Raman spectroscopy analysis.

Such vacancy density (defects) are correlated with the band gap energy of the material (Fig. 2ii). Fig. 2b shows the Tauc plot obtained from the absorption spectra of the CeO₂ samples. The Tauc plot determines the band gap energy (E_g) of all samples from the intercept on the abscissa axis of a linear fit of the (αhν)^x vs wavelength energy plot, where α is the absorbance and hν is the photon energy, considering an

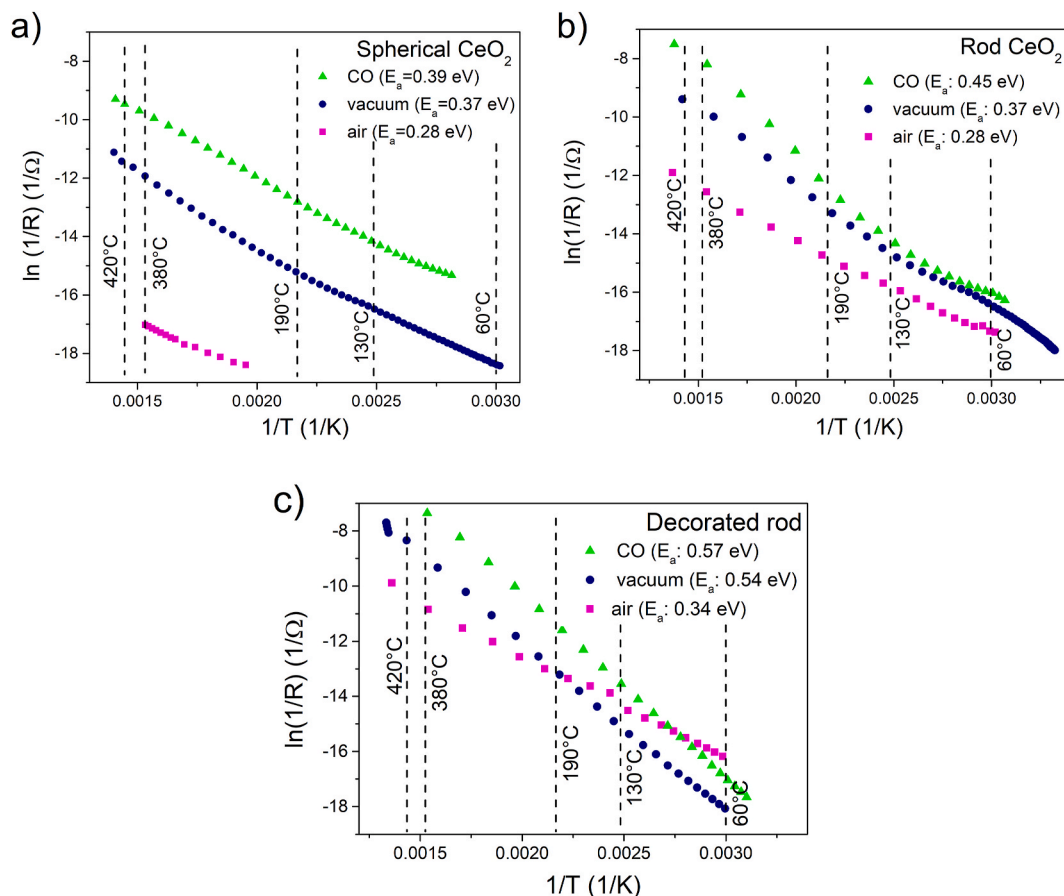


Fig. 4. Arrhenius plot for a) spherical, b) rod-like, and c) decorated rod-like CeO₂ samples.

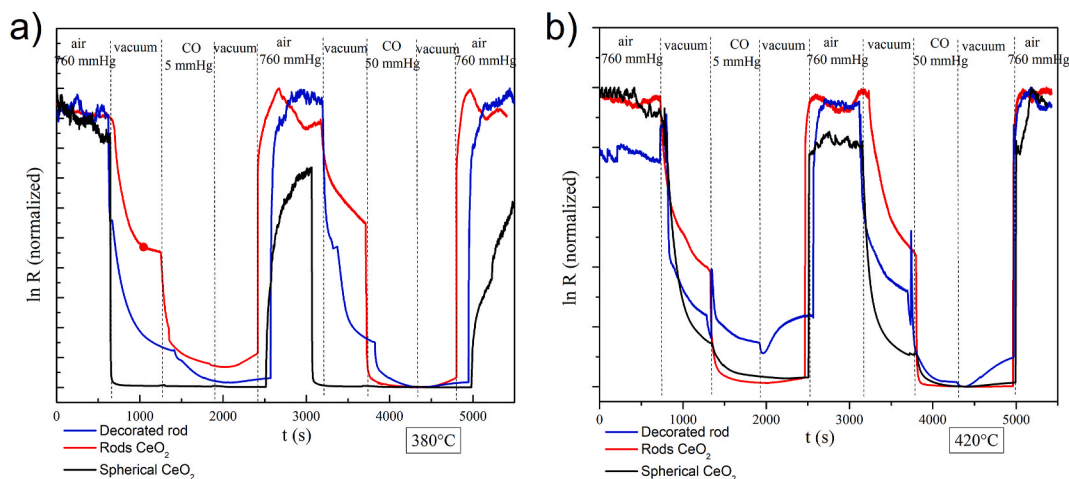


Fig. 5. Resistance as a function of time and atmosphere for pure and decorated CeO₂ samples.

indirect band gap for the pure CeO₂ [56] and a direct band gap for the decorated CeO₂ sample [8]. An E_g value of ~2.6 eV was found for all samples, which is in agreement with the literature [56] and refers to the excitation of electrons from O2p to Ce 4f. The rod-like CeO₂ sample (Fig. 2ii-b) has a slightly higher band gap energy than the spherical CeO₂ sample (Fig. 2ii-a). Considering the vacancy density in the surface type of each sample and using the theoretical band gap value (Table 1), the rod-like sample composed of the (111) and (110) surfaces presents a higher theoretical band gap value than the spherical sample formed by the (111) and (100) surfaces. For the decorated CeO₂ sample, two values were found (Fig. 2ii-c); one was due to the CeO₂ phase and other to the presence of the nickel oxide phase, which is comparable to that found by Zhao et al. [50], who observed a similar shape for the curve in the reflectance spectrum when studying TiO₂/Ni₂O₃ heterojunctions.

Fig. 3 displays the XPS analyses of spherical (Figures a), rod-like (Figures b) and decorated rod-like (Figures c) CeO₂ samples. The survey spectra are shown in Fig. 3i. For the decorated rod-like sample (Fig. 3i-c), it is possible to observe the presence of nickel with an approximate percentage similar to that used in the synthesis (5.0 (w/w)%). The Ce 3d spectrum is presented in Fig. 3ii. The presence of mixed Ce⁴⁺ and Ce³⁺ oxidation states is commonly found, as evidenced by the spin-orbit multiplets [57,58]. The fitted peaks denoted as u and v are related to the spin-orbit coupling of 3d_{3/2} and 3d_{5/2}, respectively. The doublets named as u'/v' and u₀/v₀ are due to primary photoemission from Ce(III) and its shakedown, respectively. The doublets designated as u'''/v''' and u/v-u''/v'' are assigned to primary photoemission from Ce (IV) and its shakedown features, respectively. The transfer of electrons (one or two) from a filled O 2p orbital to an empty Ce 4f orbital during the photoemission results in shakedown features [59,60]. The relative areas of each component belonging to the corresponding oxidation states (Ce³⁺ and Ce⁴⁺) determine the relative concentration of the Ce (III) oxidation state (Eq. (3)).

$$\%Ce(III) = \frac{Area\ Ce^{3+}}{(Area\ Ce^{3+} + Area\ Ce^{4+})} \times 100 \quad (3)$$

The values obtained for Ce (III) at the surface were 32.4%, 25.6% and 30.9% for spherical, rod-like, and decorated rod-like CeO₂ samples, respectively. The spherical sample had the highest presence of Ce (III), followed by the decorated rod-like sample. Comparing the pure and decorated rod-like samples, an increase of ~5% in Ce (III) was found for the decorated rod. The presence of both Ce valence states in the samples can be explained based on several factors, such as the effect of irradiation [59], lattice doping [9], particle average size [61], and exposed surface [18]. In our case, for the spherical sample the smaller particle size (Table 1 and Fig. S4) increased the density of interfacial

imperfections as one-dimensional defects (edge and line dislocations). As a result, there was a greater presence of point defects with Ce–O undercoordination, thus increasing the proportion of Ce (III). For the decorated sample, based on the DFT results it can be deduced that clusters of nickel oxide grown above the CeO₂ surface act in the reduction of Ce (IV) cations due to the appearance of acceptor energy levels. This perspective will be further studied by ab initio calculations shown in section 3.4. Fig. 3iii displays the O 1s and Ni 2p spectra. The O1s spectra of the pure CeO₂ sample were deconvoluted into three peaks: ~529, ~531 and ~532 eV, which are related to the Ce–O bond, hydroxide/surface defects (–OH, V_o) and oxygen-bonded carbon species (C–O, C = O), respectively [62,63]. For the decorated CeO₂ sample spectra, the same peaks can be observed plus an additional one at 527 eV, ascribed to the O–Ni bond. The Ni 2p spectra (inset in Fig. 3c) are displayed in the region of 865–850 eV, corresponding to the Ni 2p_{3/2} and its shakeup peaks. As reported by Oswald et al. [64], the shape of this peak can be characteristic of a Ni (III)/Ni (II) mixture, which is expected since the Ni₂O₃ particles grown on rod-like CeO₂ particles can present different types of defects. However, a greater presence of Ni(III) is verified, Fig. S5, when analyzing the Ni LVV Auger lines with emission at 390 eV, which is characteristic of Ni(III) (L2VV) [65,66].

3.2. Electrical characteristics

The temperature dependence of conductivity (G) is shown in Fig. 4, where it is possible to observe the variation of conductance as a function of inverse temperature (T⁻¹) for pure spherical (a), pure rod-like (b) and decorated rod-like (c) CeO₂ samples. The activation energy for hopping conduction adopts the form shown in Eq. (4).

$$G = (A/T)\exp(-E_a/kT), \quad (4)$$

where G is the electrical conductance, T is the temperature, E_a is the activation energy, and k is the Boltzman constant. The prefactors (A) and activation energies (E_a) can be estimated using Eq. (4) for the three different atmospheric conditions. The values obtained in the present study for the same atmospheres show that E_a for the decorated sample is higher than for the pure samples (spherical and rod-like). These results indicate that the electrons in the decorated CeO₂ sample have lower mobility to migrate from one site to an adjacent one by a hopping mechanism of conduction.

In Fig. 4c, it can be observed that at temperatures lower than ~190 °C the conductivity in air for the decorated sample is higher than in vacuum. The conduction is determined by the mobility and the density of the carriers [67]. The explanation for this fact will be better explored in the following section based on the adsorption mechanism for

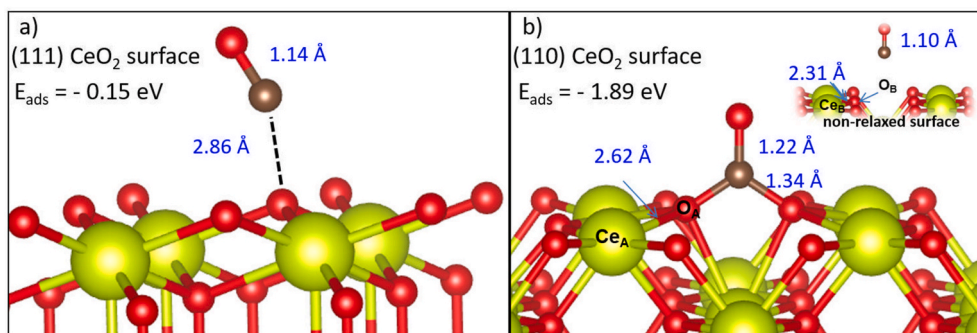


Fig. 6. CO adsorption on (111) and (110) CeO₂ surfaces. The images show the bonding distances between Ce, O and C atoms and adsorption energies. The inset of Figure b displays the non-relaxed (110) surface (i.e., before DFT simulation).

Table 2

Results of the response time obtained by resistance as a function of time and atmosphere at 380 °C and 420 °C.

	Spherical CeO ₂		Rod CeO ₂		Decorated rod	
	380 °C	420 °C	380 °C	420 °C	380 °C	420 °C
Response time (s) (5 mmHg CO gas)	609	349	245	108	397	329
Response time (s) (50 mmHg CO gas)	565	243	22	17	291	223

heterojunction.

Gas-sensing tests were performed by exposing the pure and decorated CeO₂ samples at 380 °C and 420 °C, according to Fig. 5a and b, respectively. The results of the transient response characteristics towards vacuum and carbon monoxide (at 5 mmHg and 50 mmHg of gas) are also displayed. It can be seen that after two cycles of exposure to air, vacuum and CO, the sensors recover their initial resistance, indicating that all films have good reversibility. Regarding the sensor response magnitude, it does not change substantially by increasing the concentration of CO in all samples. This could suggest that the sensors reached gas saturation. Fig. 5 also shows the electric resistance behavior of the samples. It can be observed that the electric resistance of the rod-type samples (pure and decorated) decreases abruptly with the injection of vacuum and CO gas, and then increases rapidly and recovers to its initial value after the test gas is released. However, when the films are exposed to vacuum, the electrical response of the decorated CeO₂ sample is higher than that of the pure CeO₂ sample. This can be attributed to the microstructure of the decorated sample, which presents a greater number of defects (XPS results) than the pure rods, thus presenting a greater response to vacuum.

Conversely, even though films conformed with spherical particles have a good response to vacuum, such response is not so expressive in relation to the subsequent exposure to CO. This is due to the interaction between the gas and the type of surface existing in the material. The spherical particles mainly have a solid/atmosphere interface composed of the (111) surface, while the sample with rod-type particles present a solid/atmosphere interface predominantly formed by the (111) and (110) surfaces (Fig. 1). Through computer simulations, it was observed that the (110) surface has higher adsorption energy of CO gas than the (111) surface. Fig. 6 shows the simulation of CO gas adsorption on both surfaces, (111) and (110). On the (111) surface (Fig. 6a), the low value of adsorption energy (-0.15 eV) indicates weak interaction. The distance between the C and the O closest to the surface was 2.86 Å, which is characteristic of physisorption, as also observed by other studies [19, 68]. On the other hand, the adsorption of CO on the (110) surface (Fig. 6b) reveals a more stable adsorption energy value (-1.89 eV). In this case, the geometry of both adsorbate (CO molecule) and adsorbent

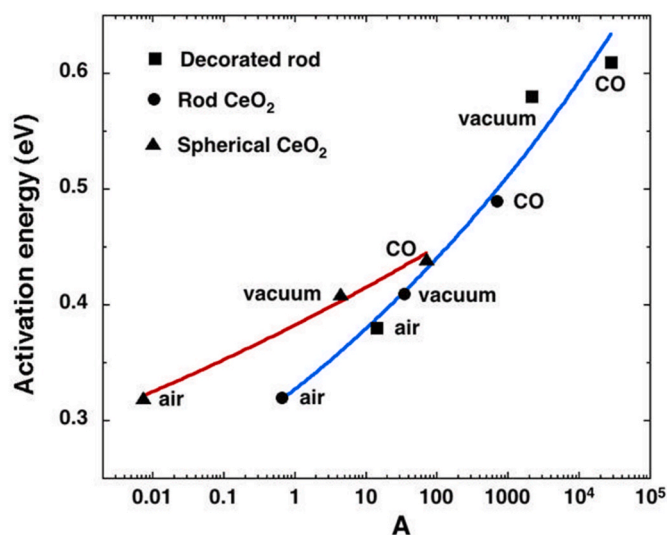


Fig. 7. Variation of effective activation energy with the prefactor, A.

(CeO₂ surface) is changed. By comparing the DFT simulation before (inset of Fig. 6b) and after surface relaxation (Fig. 6b), it can be noted that there are increases in the bonding distances between the C and O of the CO molecule of <0.12 Å and between the Ce and O bonded to the CO molecule (i.e., before after relaxation: Ce_B-O_B → Ce_A-O_A) of 0.31 Å. Both are chemisorption characteristics, which help to explain the better response to CO gas presented by the rod-type particle in comparison with the spherical sample.

The main results of this analysis are shown in Table 2, which compares the pure (spheres and rods) and decorated CeO₂ samples. The response time, defined as the time required to reach 90% of the final equilibrium value, is described. It is observed that the response time of the CeO₂ decorated with nickel oxide is higher than that of the pure sample. By comparing the morphology between the pure CeO₂ samples (rod-like and spherical), it can be noted that the former presents a shorter response time. In particular, the electrical response time for the decorated rod is much less sensitive to CO than the pure rod, suggesting that the CO begins to saturate in the decorated sample at lower concentrations.

From a comparison between the morphologies in Fig. 5 (spheres vs rods), better sensor responses can be observed for the sample with rod-like morphology in relation to the spherical morphology. Other works [8,69,70] also obtained CeO₂ nanoparticles but without a defined morphology, reaching a sensor response time between 45 and 56 s (using operating temperatures and CO concentration equal to or greater than those used in this work). In other words, when a specific morphology of CeO₂ was used, the response time decreased. Therefore,

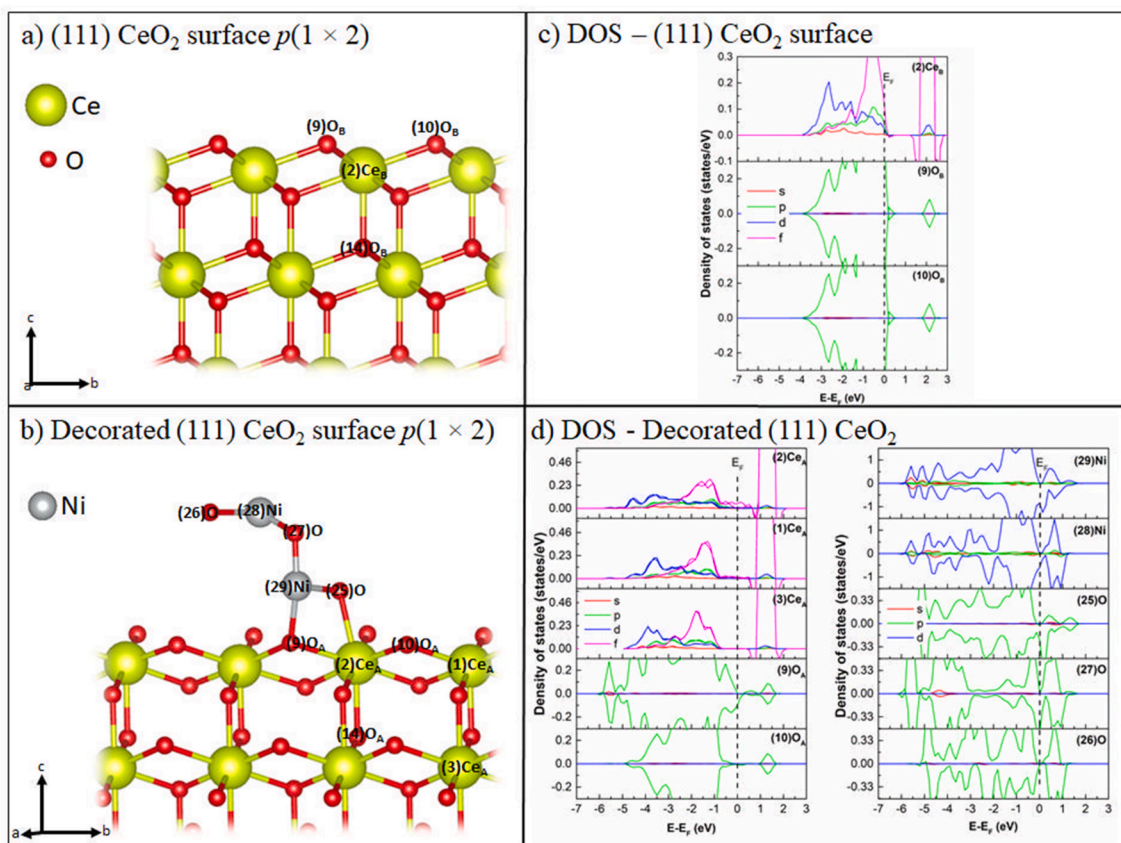


Fig. 8. Formation of the decorated CeO_2 , a) supercell (1×2) of the (111) CeO_2 surface, b) supercell interacting with Ni_2O_3 , and density of state for Ce, O, and Ni atoms of c) pure and d) decorated surfaces.

sample morphology is crucial in sensor behavior due to the different oxygen diffusion processes into and out the particles, which are responsible for annihilating or generating oxygen vacancies, as shown in previous works [17]. This is correlated with the Ce (III)/Ce (IV) concentration, and consequently with carrier concentration.

Finally, assuming that electrical conductivity is an activated process and using Eq. (04) [1] in order to gain confidence on previous analyses, we plotted effective activation energy vs prefactor, A, to show a clear relationship between the prefactors and activation energies for different samples and atmospheres (Fig. 7). Directly related to the number of carriers (electrons in the Ce 4f states, $4f^1$), prefactors can be compared with samples of similar morphologies, such as pure and decorated rod-like nanoparticles. As abovementioned, the number of electrons available for conductivity is determined by the density of vacancies. From Fig. 6, it can be deduced that the number of vacancies increases when the material is exposed to the following sequence of atmospheres: air, vacuum and CO. According to this figure, it is clearly seen that the oxygen vacancy density is always larger for the sample decorated with nickel oxide. Additionally, it is well known that the activation energy increases with the vacancy density. When studying CeO_2 single crystals with different stoichiometry, Tuller et al. [1] related vacancy density to local atomic order and changes in the lattice parameter. By comparing

Table 3
Bonding distance between Ce–O atoms for pure and decorated (111) CeO_2 surfaces.

	pure (111) CeO_2 surface (Å)	Decorated (111) CeO_2 surface (Å)
(2)Ce – (9)O	2.34	2.38
(2)Ce – (10)O	2.34	2.33
(2)Ce – (14)O	2.36	2.47

pure and decorated rod-like samples, it becomes evident that this interpretation is consistent with the lattice order and cell volume shown in Table S1. In addition, the XPS results for rod-like samples point to a larger number of Ce (III) in the decorated sample (see section 3.1).

Finally, it is worth noting that an energy widening of the cerium 4f state distribution for the decorated sample could change the electronic distribution. Moreover, the cerium 4f states appear closer to the valence band according to the UV–Vis results, suggesting that the decoration with Ni_2O_3 could cause a greater dispersion of the possible $4f^0$ states (Ce (IV)) to which electrons could jump from a $4f^1$ state now deeper in energy, Ce (III). As a consequence, an increase in the effective activation energy for CeO_2 – Ni_2O_3 samples is expected. A similar phenomenon takes place when samples are treated with reducing gases (CO treatment). The opposite occurs when vacancies are annihilated by exposing the samples to an oxygen atmosphere, followed by Ce (III) amount reduction. It can then be concluded that the DFT, XPS, UV-VIS and electronic characterizations are all consistent.

3.3. Decorated rods based on DFT simulations

In order to further explore the $\text{CeO}_2/\text{Ni}_2\text{O}_3$ heterojunction experimentally obtained and study the possible energy widening of the cerium 4f state distribution for this sample, heterojunctions of nickel oxide clusters on the (111) CeO_2 surface were theoretically constructed. In this topic, when we refer to "pure surface", it is not necessarily correlated with the experimentally obtained pure samples (spheres or rods), but with the CeO_2 surface on which nickel oxide clusters were grown. Therefore, the (111) CeO_2 surface was chosen with the purpose of reproducing the experimental findings. Ni_2O_3 clusters were placed on a surface expansion of $p(1 \times 2)$, which was found to be the most stable expansion similar to that experimentally obtained (Fig. S6). The pure

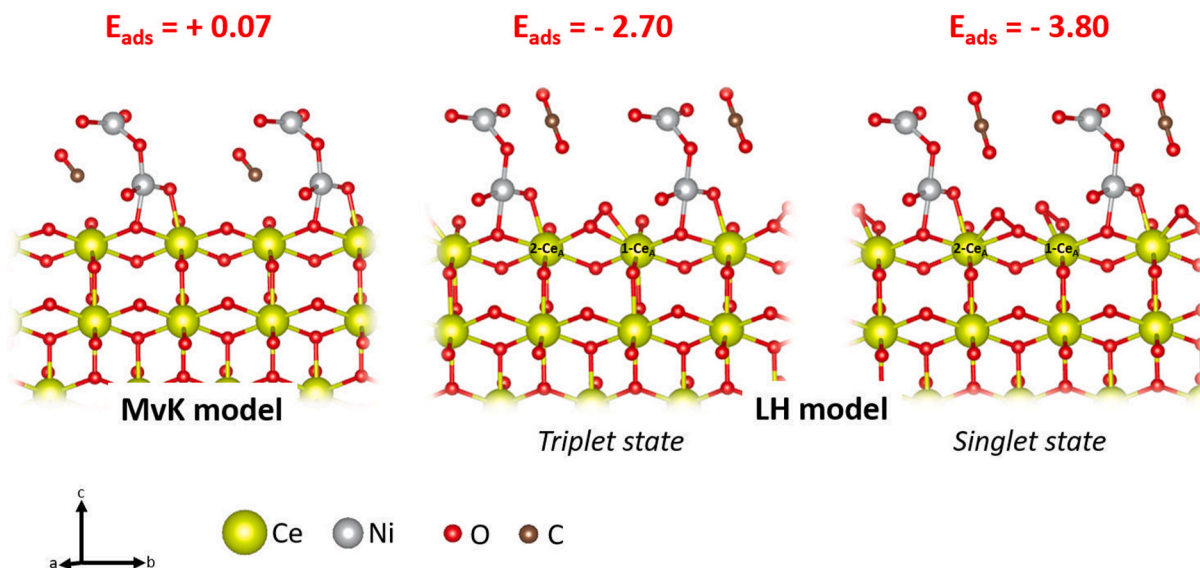


Fig. 9. CO adsorption at the $\text{CeO}_2(111)/\text{Ni}_2\text{O}_3$ heterojunction following a) MvK and b,c) LH models. b) Triplet- and c) singlet-oxygen adsorption.

(111) CeO_2 surface (Fig. 8a) and the interaction with Ni_2O_3 clusters (Fig. 8b) were analyzed. From the density of states (DOS) analysis, it can be observed that for the pure surface there is a main participation of the O-2p states at the valence band maximum (VBM) and the presence of the Ce-4f states ~ 2 eV above the VBM (Fig. 8c).

By comparing the Ce before (Ce_B) and after (Ce_A) heterojunction formation, it is possible to observe an increase in the Ce–O bond length nearest to Ni (Table 3), possibly due to the variation in the oxidation state of the cerium [71]. This structural change indicates the formation of strong covalent bond between CeO_2 and nickel oxide [72]. This was confirmed by the DOS analysis when comparing the pure (111) surface (Fig. 8c), i.e., before the existence of any heterojunctions in the sample, and the surface after decoration with nickel oxide (Fig. 8d). The comparison between Ce on the pure surface (2-Ce_B) and Ce on the heterojunction surface (Ce_A) shows a shift in the Fermi level. The cerium closest to the interface with nickel oxide, 2-Ce_A , presents f states at 0.6 eV above the Fermi level characteristic of Ce (III) [9,18], indicating that the heterojunction formation occurs by reducing the cerium atoms on the surface, which is in agreement with the electrical and XPS analyses. The more distant the Ce atoms are from the interaction with nickel oxide, the more the f states in this intermediate region decrease (1-Ce_A) until their complete disappearance (3-Ce_A), evidencing the presence of Ce (IV).

Fig. 9 shows the CO adsorption on the decorated (111) CeO_2 surface using two adsorption models: Mars-Van Krevelen (MvK) (Fig. 9a) and Langmuir–Hinshelwood (LH) (Fig. 9b and c). In the first model, the CO molecule is adsorbed on the surface, whereas in the second mechanism there is a co-adsorption of the CO and O_2 molecules. Following the MvK model [22,23], the adsorption of CO in the heterojunction proved to be unstable (Fig. 9a), with adsorption energy of +0.07 eV. This is different from the physisorption behavior found on the clean (111) CeO_2 surface (Fig. 6a) and shown by other studies [19,68], which reported that for the clean surface of CeO_2 the CO adsorption by MvK has proved to be more effective. Regarding the co-adsorption along with the LH mechanism for heterojunction (see Fig. S7 for the unrelaxed position of the adsorbed molecules), in which O_2 and CO molecules participate in the interaction with the oxide surface, a high exothermic process was observed, with an adsorption energy of -2.70 eV and -3.80 eV (Fig. 9b and c). Recent studies developed by Zhou et al. [23] demonstrated that in comparison with MvK the LH mechanism is less effective in adsorbing CO on pure CeO_2 surfaces. However, our findings for the $\text{CeO}_2/\text{Ni}_2\text{O}_3$ structure were different for pure CeO_2 . We observed that one of the oxygens that

participate in the adsorption is captured by the crystalline lattice, changing the surface clusters. Therefore, O_2 molecules have a more effective participation in the decorated sample than in the pure samples, consequently reflecting the electrical behavior observed in Fig. 4c. For temperatures below 190°C , the slope of the curve for the sample exposed to air is smaller than its exposed to CO or vacuum, meaning lower electrical resistance, that is, a different behavior in relation to pure samples. Depending on the working temperature, oxygen adsorbs as different species, i.e., molecular species ($\text{O}_{2,\text{ads}}$ or $\text{O}_{2,\text{ads}}^-$) at low temperatures ($150^\circ\text{C} < T < 200^\circ\text{C}$), or as atomic ions (O_{ads}^- or $\text{O}_{\text{ads}}^{2-}$) at higher temperatures ($200^\circ\text{C} < T < 400^\circ\text{C}$) [73]. Such species act as electron traps from 4f states of Ce, thus increasing electrical resistance. However, as previously reported below 190°C the decorated sample undergoes a reduction in electrical resistance as a result of the type of interaction between the gas and the surface present in the material. Below this temperature, there is greater participation of molecular oxygens ($\text{O}_{2,\text{ads}}$ or $\text{O}_{2,\text{ads}}^-$) present in the atmosphere (compared to ionic species, O_{ads}^- or $\text{O}_{\text{ads}}^{2-}$, found above 190°C), leaving more free electrons in the f states of Ce, consequently reducing the electrical resistance in this temperature range. Nevertheless, even though this could also occur in the pure samples (Fig. S8), it was found that the decorated sample is more sensitive to the adsorption of O_2 molecules (Fig. 9b and c).

In order to confirm which is the most favorable state for the adsorption of the O_2 molecule, the two possible states of adsorption, singlet and triplet, were evaluated. For the LH model, the adsorption processes of both singlet- and triplet- O_2 adsorption were proposed to dissociate the heterojunction surface. For the triplet state of O_2 , it was observed that O–O bond breaking occurs in Ce–O bonds, denoted as 1Ce-A . As previously observed, this site has a more Ce (IV) character than Ce (III), while for the dissociation process of singlet O_2 a O–O bond breaking occurs in the 2Ce-A site, which has a more Ce (III) character. These results suggest that the CO gas adsorption mechanism on the surface of Ni_2O_3 -decorated CeO_2 follows an LH mechanism and that singlet- and triplet-oxygen states are possible to occur with greater adsorption stability for the singlet state. Therefore, it is assumed that the behavior of higher conductivity of the heterojunction observed experimentally for lower analysis temperatures (Fig. 4c) is related to the greater ease of adsorption of the O_2 and CO molecules at such heterojunction.

4. Conclusions

Pure CeO₂ samples with different morphologies (spherical and rod-like) and CeO₂ nanorods decorated with nickel oxide were synthesized and evaluated structurally and electrically. Structural and morphological analyses showed that the morphology of the pure spherical CeO₂ was mainly constituted of the (111) surfaces with a high concentration of Ce (III) resulting from the smaller particle size. The pure rod-like sample presented a predominance of the (111) and (110) surfaces and a lower proportion of Ce (III). The heterojunction formation revealed a nickel oxide growth decorating the CeO₂ rods without change in morphology with respect to the pure rod-like sample. The cubic phase of CeO₂ led to the growth of the hexagonal phase of Ni₂O₃ stoichiometry for the nickel oxide. The results obtained by Raman scattering and diffuse reflectance spectroscopies evidenced the relationship between the type of surface present in each sample and defect density. Electrical analyses demonstrated an increase in activation energy for the nickel oxide-decorated sample in comparison with pure rods, with a consequent increase in the electrical conductance for a temperature below 190 °C in air atmosphere compared to the other atmospheres analyzed. From a comparison between the pure samples (rods and spheres), it was observed that the adsorption of CO gas was higher in the rod-like sample due to the different adsorption energies of its surfaces. The activation energy, the increase in vacancy density, and the local atomic order of the pure and decorated rod-like samples were correlated with prefactor A, which can be directly associated with the number of carriers in the sample. The adsorption mechanism for the decorated sample was also distinct from that of the pure sample. DFT simulation analysis revealed that the adsorption of CO gas on the decorated surface followed an LH adsorption mechanism. This mechanism was different for the pure surface and could explain the increase in conductivity at lower analysis temperatures for the sample obtained as a heterojunction. We expect that this experimental/theoretical evidence on the relationship between pure and decorated surfaces will open up new paths for the controlled synthesis of materials with highly tuned properties for applications using surface science.

Declaration of competing interest

The authors declare that they have no known competing financial interests or personal relationships that could have appeared to influence the work reported in this paper.

Acknowledgments

The authors acknowledge the CEPID/CDMF, the São Paulo Research Foundation (FAPESP) (Proc. Nos. 2013/07296-2, 2019/09296-6 and 2017/19143-7), and the National Council for Scientific and Technological Development (CNPq). This research was supported by LNLS - Brazilian Synchrotron Light Laboratory, Research LMF - 24859, CNPEM/MCTIC. J.A. acknowledges Universitat Jaume I (project UJI-B2019-30) and the Ministerio de Ciencia, Innovación y Universidades (project PGC2018094417-B-I00).

Appendix A. Supplementary data

Supplementary data to this article can be found online at <https://doi.org/10.1016/j.ceramint.2022.01.286>.

References

- [1] H.L. Tuller, A.S. Nowick, Small polaron electron transport in reduced CeO₂ single crystals, *J. Phys. Chem. Solid.* 38 (1977) 859–867.
- [2] H.L. Tuller, A.S. Nowick, Defect structure and electrical properties of nonstoichiometric CeO₂ single crystals, *J. Electrochem. Soc.* 126 (1979) 209.
- [3] H. Yahiro, Y. Baba, K. Eguchi, H. Arai, High Temperature fuel cell with ceria-yttria solid electrolyte, *J. Electrochem. Soc.* 135 (1988) 2077.
- [4] R.A.C. Amoresi, R.C. Oliveira, N.L. Marana, P.B. de Almeida, P.S. Prata, M. A. Zaghe, E. Longo, J.R. Sambrano, A.Z. Simoes, CeO₂ nanoparticle morphologies and their corresponding crystalline planes for the photocatalytic degradation of organic pollutants, *ACS Appl. Nano Mater.* 2 (2019) 6513–6526.
- [5] D. Channei, B. Inceesungvorn, N. Wetchakun, S. Ukritnukun, A. Nattestad, J. Chen, Photocatalytic degradation of methyl orange by CeO₂ and Fe-doped CeO₂ films under visible light irradiation, *Sci. Rep.* 4 (2014) 5757, <https://doi.org/10.1038/srep05757>.
- [6] H. Gu, M.D. Soucek, Preparation and characterization of monodisperse cerium oxide nanoparticles in hydrocarbon solvents, *Chem. Mater.* 19 (2007) 1103–1110.
- [7] S. Tsunekawa, T. Fukuda, A. Kasuya, Blue shift in ultraviolet absorption spectra of monodisperse CeO_{2-x} nanoparticles, *J. Appl. Phys.* 87 (2000) 1318–1321.
- [8] P.P. Ortega, L.S.R. Rocha, J.A. Cortés, M.A. Ramirez, C. Buono, M.A. Ponce, A. Z. Simões, Towards carbon monoxide sensors based on europium doped cerium dioxide, *Appl. Surf. Sci.* 464 (2019) 692–699, <https://doi.org/10.1016/j.apsusc.2018.09.142>.
- [9] L.S.R. Rocha, R.A.C. Amoresi, T. Marinho, N. Letícia, J. Ricardo, C. Manuel, A. Zirpoli, M. Adolfo, E. Longo, Experimental and theoretical interpretation of the order/disorder clusters in CeO₂:La, *Appl. Surf. Sci.* 510 (2020) 145216, <https://doi.org/10.1016/j.apsusc.2019.145216>.
- [10] A. Trovarelli, Catalytic properties of ceria and CeO₂-containing materials, *Catal. Rev.* 38 (1996) 439–520.
- [11] R. Schmitt, A. Nanning, O. Kraynis, R. Korobko, A.I. Frenkel, I. Lubomirsky, S. M. Haile, J.L.M. Rupp, A review of defect structure and chemistry in ceria and its solid solutions, *Chem. Soc. Rev.* 49 (2020) 554–592.
- [12] M.F. Al-Kuhaili, S.M.A. Durrani, I.A. Bakhtiari, Carbon monoxide gas-sensing properties of CeO₂-ZnO thin films, *Appl. Surf. Sci.* 255 (2008) 3033–3039, <https://doi.org/10.1016/j.apsusc.2008.08.058>.
- [13] N. Izu, T. Itoh, M. Nishibori, I. Matsubara, W. Shin, Chemical Effects of noble metal addition on response of ceria thick film CO sensors, *Sensor. Actuator. B Chem.* 171–172 (2012) 350–353, <https://doi.org/10.1016/j.snb.2012.04.058>.
- [14] R.C. Deus, R.A.C. Amoresi, P.M. Desimone, F. Schipani, L.S.R. Rocha, M.A. Ponce, A.Z. Simoes, E. Longo, Electrical behavior of cerium dioxide films exposed to different gases atmospheres, *Ceram. Int.* 42 (2016) 15023–15029, <https://doi.org/10.1016/j.ceramint.2016.06.151>.
- [15] L. Liao, H.X. Mai, Q. Yuan, H.B. Lu, J.C. Li, C. Liu, C.H. Yan, Z.X. Shen, T. Yu, Single CeO₂ nanowire gas sensor supported with Pt nanocrystals: gas sensitivity, surface bond states, and chemical mechanism, *J. Phys. Chem. C* 112 (2008) 9061–9065, <https://doi.org/10.1021/jp7117778>.
- [16] L.S.R. Rocha, M. Gilense, M.A. Ponce, C.M. Aldao, L.L. Oliveira, E. Longo, A. Z. Simoes, Novel gas sensor with dual response under CO(g) exposure: optical and electrical stimuli, *Phys. B Condens. Matter* 536 (2017) 280–288, <https://doi.org/10.1016/j.physb.2017.10.083>.
- [17] L.S.R. Rocha, F. Schipani, C.M. Aldao, L. Cabral, A.Z. Simoes, C. Macchi, G. E. Marques, M.A. Ponce, E. Longo, Experimental and ab initio studies of deep-bulk traps in doped rare-earth oxide thick films, *J. Phys. Chem. C* 124 (2019) 997–1007, <https://doi.org/10.1021/acs.jpcc.9b07217>.
- [18] M. Nolan, S. Grigoleit, D.C. Sayle, S.C. Parker, G.W. Watson, Density functional theory studies of the structure and electronic structure of pure and defective low index surfaces of ceria, *Surf. Sci.* 576 (2005) 217–229, <https://doi.org/10.1016/j.susc.2004.12.016>.
- [19] M. Nolan, S.C. Parker, G.W. Watson, Vibrational properties of CO on ceria surfaces, *Surf. Sci.* 600 (2006) L175–L178, <https://doi.org/10.1016/j.susc.2006.05.015>.
- [20] S.-H. Zhong, G. Lu, X.-Q. Gong, A DFT+U study of the structures and reactivities of polar CeO₂ (100) surfaces, *Chin. J. Catal.* 38 (2017) 1138–1147.
- [21] M. Eiswirth, J. Bürger, P. Strasser, G. Ertl, Oscillating Langmuir–hinselwood mechanisms, *J. Phys. Chem.* 100 (1996) 19118–19123.
- [22] C. Doornkamp, V. Ponc, The universal character of the Mars and Van Krevelen mechanism, *J. Mol. Catal. Chem.* 162 (2000) 19–32, [https://doi.org/10.1016/S1381-1169\(00\)00319-8](https://doi.org/10.1016/S1381-1169(00)00319-8).
- [23] C. Zhou, D. Wang, X. Gong, A DFT+U revisit of reconstructed CeO₂ (100) surfaces: structures, thermostabilities and reactivities, *Phys. Chem. Chem. Phys.* 2 (2019) 17–20, <https://doi.org/10.1039/C9CP03408K>.
- [24] R. Cristina de Oliveira, R.A. Pontes Ribeiro, G.H. Cruvinel, R.A. Ciola Amoresi, M. H. Carvalho, A.J. Aparecido de Oliveira, M. Carvalho de Oliveira, S. Ricardo de Lazaro, L. Fernando da Silva, A.C. Catto, Role of surfaces in the magnetic and ozone gas-sensing properties of ZnFe₂O₄ nanoparticles: theoretical and experimental insights, *ACS Appl. Mater. Interfaces* 13 (2021) 4605–4617.
- [25] M.C. dos Santos, L. Lucchetti, J. Almeida, P.A. da Silva Aurturo, Assessing the oxygen reduction reaction by a 2-electron mechanism on ceria surfaces, *Phys. Chem. Chem. Phys.* 23 (2021) 18580–18587, <https://doi.org/10.1039/D1CP03007H>.
- [26] L.S.R. Rocha, R.A.C. Amoresi, H. Moreno, M.A. Ramirez, M.A. Ponce, C.R. Foschini, E. Longo, A.Z. Simoes, Novel approaches of nanoceria with magnetic, photoluminescent, and gas-sensing properties, *ACS Omega* 5 (2020) 14879–14889.
- [27] C. Xu, P.R. Anusuyadevi, C. Aymonier, R. Luque, S. Marre, Nanostructured materials for photocatalysis, *Chem. Soc. Rev.* 48 (2019) 3868–3902.
- [28] M. Radecka, K. Zakrzewska, TiO₂/SnO₂ gas sensors of H₂, *Int. Sci. Conf. Optoelectron. Electron. Sensors.* (2018) 1–4, <https://doi.org/10.1109/COE.2018.8435174>.
- [29] W. Zeng, T. Liu, Z. Wang, Sensitivity improvement of TiO₂-doped SnO₂ to volatile organic compounds, *Phys. E Low-dimens. Syst. Nanostruct.* 43 (2010) 633–638.
- [30] D.E. Motaung, G.H. Mhlongo, P.R. Makgwane, B.P. Dhone, F.R. Cummings, H. C. Swart, S.S. Ray, Ultra-high sensitive and selective H₂ gas sensor manifested by interface of n–n heterostructure of CeO₂-SnO₂ nanoparticles, *Sensor. Actuator. B Chem.* 254 (2018) 984–995.

- [31] J. Liu, M. Dai, T. Wang, P. Sun, X. Liang, G. Lu, K. Shimano, N. Yamazoe, Enhanced gas sensing properties of SnO₂ hollow spheres decorated with CeO₂ nanoparticles heterostructure composite materials, *ACS Appl. Mater. Interfaces* 8 (2016) 6669–6677.
- [32] N. Jayababu, M. Poloju, J. Shruthi, M.V.R. Reddy, NiO decorated CeO₂ nanostructures as room temperature isopropanol gas sensors, *RSC Adv.* 9 (2019) 13765–13775.
- [33] G. Zhou, H. Liu, K. Cui, A. Jia, G. Hu, Z. Jiao, Y. Liu, X. Zhang, Role of surface Ni and Ce species of Ni/CeO₂ catalyst in CO₂ methanation, *Appl. Surf. Sci.* 383 (2016) 248–252.
- [34] K. Jouini, A. Raouafi, W. Dridi, M. Daoudi, B. Mustapha, R. Chtourou, F. Hosni, Investigation of gamma-ray irradiation induced phase change from NiO to Ni₂O₃ for enhancing photocatalytic performance, *Optik* 195 (2019) 163109.
- [35] X. Zhang, V. Stevanović, M. d’Avezac, S. Lany, A. Zunger, Prediction of A₂BX₄ metal-chalcogenide compounds via first-principles thermodynamics, *Phys. Rev. B* 86 (2012) 14109.
- [36] P.S. Aggarwal, A. Goswami, An oxide of tervalent nickel, *J. Phys. Chem.* 65 (1961) 2105.
- [37] Y. Li, Z. Wei, M. Ding, L. Ma, X. Zhu, J. Liang, Synthesis and electrochemical properties of nickel oxide coated ZnMn₂O₄ nanocomposites, *J. Ceram. Soc. Japan.* 127 (2019) 747–753.
- [38] M. Rani, U. Shanker, Sun-light driven rapid photocatalytic degradation of methylene blue by poly (methyl methacrylate)/metal oxide nanocomposites, *Colloids Surf. A Physicochem. Eng. Asp.* 559 (2018) 136–147.
- [39] H. Zhang, Z. Ji, T. Xia, H. Meng, C. Low-Kam, R. Liu, S. Pokhrel, S. Lin, X. Wang, Y.-P. Liao, Use of metal oxide nanoparticle band gap to develop a predictive paradigm for oxidative stress and acute pulmonary inflammation, *ACS Nano* 6 (2012) 4349–4368.
- [40] X.W. Jian Wang, Yang Pan, The high-performance, room-temperature and No-Humidity-Impact ammonia sensor based on heterogeneous nickel oxide and zinc oxide nanocrystals, *ACS Appl. Mater. Interfaces* 7 (2015) 3816–3824, <https://doi.org/10.1021/am508807a>.
- [41] M. Bao, Y. Chen, F. Li, J. Ma, T. Lv, Y. Tang, L. Chen, Z. Xu, T. Wang, Plate-like p-n heterogeneous NiO/WO₃ nanocomposites for high performance room temperature NO₂ sensors, *Nanoscale* 6 (2014) 4063–4066, <https://doi.org/10.1039/c3nr05268k>.
- [42] W. Zou, C. Ge, M. Lu, S. Wu, Y. Wang, J. Sun, Y. Pu, C. Tang, F. Gao, L. Dong, Engineering the NiO/CeO₂ interface to enhance the catalytic performance for CO oxidation, *RSC Adv.* 5 (2015) 98335–98343, <https://doi.org/10.1039/C5RA20466F>.
- [43] G. Kresse, J. Furthmüller, J. Hafner, Theory of the crystal structures of selenium and tellurium: the effect of generalized-gradient corrections to the local-density approximation, *Phys. Rev. B* 50 (1994) 13181.
- [44] G. Kresse, J. Furthmüller, Efficiency of ab-initio total energy calculations for metals and semiconductors using a plane-wave basis set, *Comput. Mater. Sci.* 6 (1996) 15–50.
- [45] P.R.L. Keating, D.O. Scanlon, B.J. Morgan, N.M. Galea, G.W. Watson, Analysis of intrinsic defects in CeO₂ using a Koopmans-like GGA+U approach, *J. Phys. Chem. C* 116 (2012) 2443–2452.
- [46] S.L. Dudarev, G.A. Botton, S.Y. Savrasov, C.J. Humphreys, A.P. Sutton, Electron-energy-loss spectra and the structural stability of nickel oxide: an LSDA+ U study, *Phys. Rev. B* 57 (1998) 1505.
- [47] W.-B. Zhang, N. Yu, W.-Y. Yu, B.-Y. Tang, Stability and magnetism of vacancy in NiO: a GGA+ U study, *Eur. Phys. J. B.* 64 (2008) 153–158.
- [48] S. Lany, J. Osorio-Guillén, A. Zunger, Origins of the doping asymmetry in oxides: hole doping in NiO versus electron doping in ZnO, *Phys. Rev. B* 75 (2007) 241203.
- [49] X. Song, L. Li, X. Chen, Q. Xu, B. Song, Z. Pan, Y. Liu, F. Juan, F. Xu, B. Cao, Enhanced triethylamine sensing performance of α-Fe₂O₃ nanoparticle/ZnO nanorod heterostructures, *Sensor. Actuator. B Chem.* 298 (2019) 126917.
- [50] W. Zhao, W. Ma, C. Chen, J. Zhao, Z. Shuai, Efficient degradation of toxic organic pollutants with Ni₂O₃/TiO_{2-x}B_x under visible irradiation, *J. Am. Chem. Soc.* 126 (2004) 4782–4783.
- [51] S. Tiwari, G. Rathore, N. Patra, A.K. Yadav, D. Bhattacharya, S.N. Jha, C.M. Tseng, S.W. Liu, S. Biring, S. Sen, Oxygen and cerium defects mediated changes in structural, optical and photoluminescence properties of Ni substituted CeO₂, *J. Alloys Compd.* 782 (2019) 689–698.
- [52] F. Dong, Y. Meng, W. Han, H. Zhao, Z. Tang, Morphology effects on surface chemical properties and lattice defects of Cu/CeO₂ catalysts applied for low-temperature CO oxidation, *Sci. Rep.* 9 (2019) 1–14.
- [53] C. Schilling, A. Hofmann, C. Hess, M. Vero, Raman spectra of polycrystalline CeO₂: a density functional theory study, *J. Phys. Chem. C* 121 (2017) 20834–20849, <https://doi.org/10.1021/acs.jpcc.7b06643>.
- [54] Z. Feng, Q. Ren, R. Peng, S. Mo, M. Zhang, M. Fu, L. Chen, D. Ye, Effect of CeO₂ morphologies on toluene catalytic combustion, *Catal. Today* 332 (2019) 177–182, <https://doi.org/10.1016/j.cattod.2018.06.039>.
- [55] W.H. Weber, K.C. Hass, J.R. McBride, Raman study of CeO₂: second-order scattering, lattice dynamics, and particle-size effects, *Phys. Rev.* 48 (1993) 178.
- [56] G. Zhou, Y. Yao, X. Zhao, X. Liu, B. Sun, A. Zhou, Band gap energies for white nanosheets/yellow nanoislands/purple nanorods of CeO₂, *RSC Adv.* 6 (2016) 59370–59374.
- [57] D.R. Mullins, S.H. Overbury, D.R. Huntley, Electron spectroscopy of single crystal and polycrystalline cerium oxide surfaces, *Surf. Sci.* 409 (1998) 307–319.
- [58] B.M. Reddy, A. Khan, Y. Yamada, T. Kobayashi, S. Loridant, J.-C. Volta, Surface characterization of CeO₂/SiO₂ and V₂O₅/CeO₂/SiO₂ catalysts by Raman, XPS, and other techniques, *J. Phys. Chem. B* 106 (2002) 10964–10972.
- [59] J.P. Holgado, R. Alvarez, G. Munuera, Study of CeO₂ XPS spectra by factor analysis: reduction of CeO₂, *Appl. Surf. Sci.* 161 (2000) 301–315.
- [60] L. Truffault, M. Magnani, P. Hammer, C. V Santilli, S.H. Pulcinelli, Structural and optical features of ureasiloxane–polyethylene oxide hybrids containing CeO₂ nanoparticles, *Colloids Surf. A Physicochem. Eng. Asp.* 471 (2015) 73–80.
- [61] S. Deshpande, S. Patil, S.V.N.T. Kuchibhatla, S. Seal, Size dependency variation in lattice parameter and valency states in nanocrystalline cerium oxide, *Appl. Phys. Lett.* 87 (2005) 133113.
- [62] Y. Huang, B. Long, M. Tang, Z. Rui, M.-S. Balogun, Y. Tong, H. Ji, Bifunctional catalytic material: an ultrastable and high-performance surface defect CeO₂ nanosheets for formaldehyde thermal oxidation and photocatalytic oxidation, *Appl. Catal. B Environ.* 181 (2016) 779–787.
- [63] F. Chen, P. Ho, R. Ran, W. Chen, Z. Si, X. Wu, D. Weng, Z. Huang, C. Lee, Synergistic effect of CeO₂ modified TiO₂ photocatalyst on the enhancement of visible light photocatalytic performance, *J. Alloys Compd.* 714 (2017) 560–566.
- [64] S. Oswald, W. Brückner, XPS depth profile analysis of non-stoichiometric NiO films, *Surf. Interface Anal. An Int. J. Devoted to Dev. Appl. Tech. Anal. Surfaces, Interfaces Thin Film.* 36 (2004) 17–22.
- [65] A.N. Mansour, Characterization of NiO by XPS, *Surf. Sci. Spectra* 3 (1994) 231–238.
- [66] A.N. Mansour, C.A. Melendres, Characterization of Ni₂O₃·6H₂O by XPS, *Surf. Sci. Spectra* 3 (1994) 263–270.
- [67] F.-C. Chiu, A review on conduction mechanisms in dielectric films, *Adv. Mater. Sci. Eng.* 2014 (2014).
- [68] M. Huang, S. Fabris, CO adsorption and oxidation on ceria surfaces from DFT+U calculations, *J. Phys. Chem. C* 112 (2008) 8643–8648.
- [69] N. Izu, I. Matsubara, T. Itoh, T. Akamatsu, W. Shin, CO responses of sensors based on cerium oxide thick films prepared from clustered spherical nanoparticles, *Sensors* 13 (2013) 3252–3261.
- [70] S.M.A. Durrani, M.F. Al-Kuhaili, I.A. Bakhtiari, Carbon monoxide gas-sensing properties of electron-beam deposited cerium oxide thin films, *Sensor. Actuator. B Chem.* 134 (2008) 934–939.
- [71] T.K. Sham, L edge chemical shift and bond length difference of the mixed oxidation Ce³⁺/Ce⁴⁺ redox couple in solution, *J. Chem. Phys.* 79 (1983) 1116.
- [72] J. Carrasco, L. Barrio, P. Liu, J.A. Rodriguez, M.V. Ganduglia-Pirovano, Theoretical studies of the adsorption of CO and C on Ni (111) and Ni/CeO₂ (111): evidence of a strong metal-support interaction, *J. Phys. Chem. C* 117 (2013) 8241–8250.
- [73] A. Gurlo, Interplay between O₂ and SnO₂: oxygen ionosorption and spectroscopic evidence for adsorbed oxygen, *ChemPhysChem* 7 (2006) 2041–2052.